IEEE Access
Multidisciplinary | Rapid Review | Open Access Journal

Received October 25, 2019, accepted November 30, 2019, date of publication December 10, 2019,
date of current version December 23, 2019.

Digital Object Identifier 10.1109/ACCESS.2019.2958866

Gibbs-Phenomenon-Reduced Digital PWM for Power Amplifiers Using Pulse Modulation

SHU-CHEN LIN[1,2], SHUO-HENG XU[1], (Student Member, IEEE), YOU-HUEI CHEN[1], CHUN-WEI CHANG[3], (Member, IEEE), YI-JAN EMERY CHEN[4,5,6], (Fellow, IEEE), AND JAU-HORNG CHEN[1], (Senior Member, IEEE)

[1]Department of Engineering Science, National Taiwan University, Taipei 10617, Taiwan
[2]NanoSemi, Inc., Waltham, MA 02451, USA
[3]NXP Semiconductors, Chandler, AZ 85224, USA
[4]Graduate Institute of Electronics Engineering, National Taiwan University, Taipei 10617, Taiwan
[5]Graduate Institute of Communication Engineering, National Taiwan University, Taipei 10617, Taiwan
[6]Department of Electrical Engineering, National Taiwan University, Taipei 10617, Taiwan

Corresponding author: Jau-Horng Chen (jauchen@ntu.edu.tw)

This work was supported in part by the Ministry of Science and Technology, Taiwan, under Grant MOST 106-2221-E-002-222-MY3, Grant 106-2221-E-002-212-MY3, and Grant 108-2218-E-011-011, and in part by the Freescale Semiconductor Inc., (now NXP Semiconductors) through the National Taiwan University Yen Tjing Ling Research Institute under Contract 104-S-A37.

ABSTRACT The pulse-modulated polar transmitter (PMPT) uses radio-frequency (RF) phase modulated signal with pulse-width modulated envelope to drive a power amplifier (PA) as a switch to achieve high linearity and high efficiency. However, as the signal bandwidth increases, various non-idealities limit the performance of the PMPT architecture. In this paper, a Gibbs-phenomenon reduction filter is proposed with a partial Fourier series of digital pulse-width modulation (PWM) such that the pulsed signal is more immune to the distortion in nonlinear high-efficiency RF PAs. For validation, a prototype transmitter was tested with a 20-MHz bandwidth 256-QAM 5G new radio (NR) signal at 2.14 GHz. The proposed method achieved a drain efficiency of 28.3%, error vector magnitude (EVM) of 1.67%, and adjacent channel leakage ratio (ACLR) of -45.4 dBc at an output power of 18 dBm using the prototype transmitter. Linearity requirements for base stations were met without the use of any digital predistortion methods.

INDEX TERMS Power amplifiers, power amplifier linearization, polar transmitters, radio transmitters, microwave amplifiers.

I. INTRODUCTION

The radio-frequency (RF) power amplifier (PA) has always been the most power-consuming component in a wireless communication system. As the need of high data-rate transmission continued to grow rapidly in the recent years, modern wireless communication standards such as 4G Long Term Evolution (LTE) and 5G New Radio (NR) have been proposed. Both 4G and 5G standards utilize variations of orthogonal frequency division multiple access (OFDMA), which have very high peak-to-average power ratio (PAPR). It is well known that signals with high PAPR would lead to low PA efficiency since the PA would require more back off. In recent years, a lot of research efforts have been focused on improving PA efficiencies for OFDMA applications where PAPR is in the range of 10 dB.

Various linear high-efficiency architectures proposed in [1]–[6] have been extensively studied in the past decades. Kahn's envelope elimination and restoration (EER) is one such method. The EER polar transmitter uses a nonlinear but highly efficient PA to amplify the phase information and modulates the supply with an efficient dynamic power supply circuit, which contains the envelope information. This technique can ideally achieve 100% efficiency. However, as the signal bandwidth increases, the efficiency of the dynamic power supply drops significantly. Moreover, the delay alignment between the two paths becomes more difficult and may corrupt the signal. Hence, modification of the EER was first proposed in [7] by using delta-sigma modulation to modulate the envelope into two-level pulses before applying the RF PA where the duty cycle is proportional to the envelope magnitude. In [8], the pulse-modulated polar transmitter (PMPT) was proposed where pulse-width modulation (PWM) was used for ease of filtering the out-of-band emissions. The block diagram is shown in Fig. 1. It avoided using a dynamic power supply circuit which causes delay mismatch and high modulator power overhead issues for a wideband signal. Moreover, it operated the RF PA either in the on or off state.

The associate editor coordinating the review of this manuscript and approving it for publication was Shaoyong Zheng.

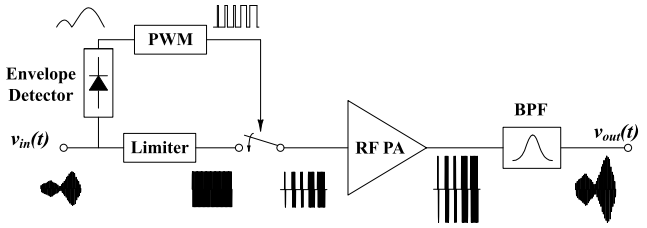

FIGURE 1. Block diagram of a pulse-modulated polar transmitter in [9]–[13].

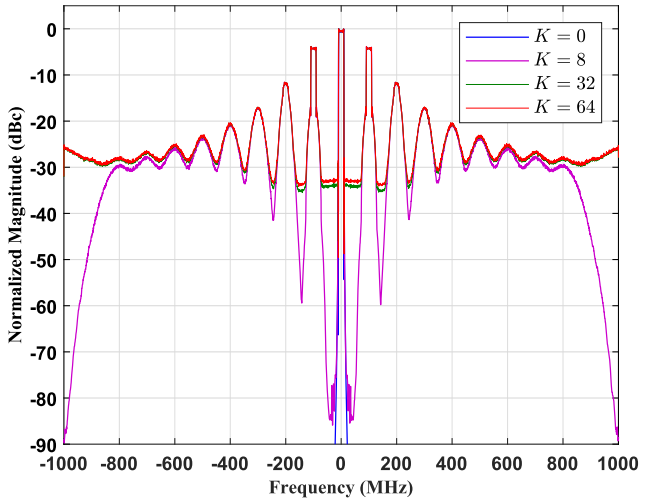

FIGURE 2. A comparison of finite number K of PFS.

The two-state operation of the RF PA can not only achieve high efficiency, but also high linearity [9]–[14].

PMPTs using conventional digital pulse-width modulation (DPWM) performed well up to 5 MHz of signal bandwidth. As the bandwidth increased, the distortion caused by the finite rise and fall times of the RF PA required predistortion to be performed [9]. Furthermore, it was identified in [10] that PWM signals suffer from aliasing effect and lead to degraded adjacent channel leakage ratio (ACLR) that cannot be linearized. Thus, the aliasing-free digital pulse-width modulation (AFDPWM) technique was proposed in [10]. However, the AFDPWM signal is no longer a two-level signal and requires linear power amplification. In [11], it was identified that AFDPWM is suitable for predistortion, which solved both the linearity and aliasing problems concurrently. It was further identified in [12] that using a wideband PA would reduce the susceptibility of AFDPWM to PA nonlinearity such that it would not require predistortion. Moreover, several techniques have been proposed in [13], [14] to increase coding efficiency and eliminate the PWM spurs, which are generated at the harmonics of the PWM sampling frequency without degrading the PA efficiency.

The aliasing problem was identified in [10] as a result of infinite series in DPWM and could be solved by using partial Fourier series (PFS) or the first few terms of a Fourier series. However, the use of PFS would lead to Gibbs phenomenon [15], which makes the modulated signal no longer a two-level signal that requires linear power amplification. Memoryless digital predistortion (DPD) was performed in [11] and [14] such that the linearity requirement of base stations were achieved. In this paper, the nonlinearity of PMPTs caused by Gibbs phenomenon is discussed. The solutions of reducing the ripples were extensively discussed in [16]–[20]. Among the various proposed methods, the spectral filter described in [16] is adapted for this work because of its simplicity even though Gibbs phenomenon cannot be fully avoided. By filtering after AFDPWM or PFS of DPWM, the bandlimited signal can be closer to a two-state waveform and be more immune to PA nonlinearity. Moreover, the additional power required for computation is negligible compared to a memoryless DPD implementation, which requires an additional RF receiver.

II. NON-IDEAL CHARACTERISTICS OF GIBBS PHENOMENON

A complex modulated baseband signal can be expressed in the polar form of

$$v_{baseband}(t) = E(t) \cdot e^{j\theta(t)}, \tag{1}$$

where the normalized amplitude is $E(t)$ and phase is $\theta(t)$. In PMPTs, the nonconstant amplitude information $E(t)$ is pulse-width modulated into two-level pulses $E_{PWM}(t)$ using DPWM. After up-conversion to the carrier frequency, the pulse-modulated RF signal will be in the form of

$$v_{RF}(t) = Re\{E_{PWM}(t) \cdot e^{j(2\pi f_c t + \theta(t))}\}, \tag{2}$$

where the RF carrier frequency is f_c. The conventional PMPTs using DPWM is linear enough to pass the spectral mask when the bandwidth of the baseband signal is narrow. As the bandwidth increases, the baseband signal after DPWM cannot achieve sufficient dynamic range unless oversampling ratio (OSR) is maintained because of the increase in quantization noise and aliasing error mentioned in [10]. If OSR is to be maintained for wideband signals, the PWM sampling frequency may be greater than the carrier frequency and makes this architecture useless. The spectral performance of DPWM has been well discussed in [21]–[23]. The aliasing-problem which cause poor spectral performance was identified and solved in [10] by using AFDPWM or PFS of DPWM. According to the analytical Fourier expression of [21], asymmetric double edge DPWM is utilized in this work because of the least in-band distortion. The PFS of the asymmetric double edge DPWM representation of an envelope signal using only the first K terms in the Fourier series has been well-derived in [10] and can be written as

$$E_{PFS,K}(t) = \sum_{k=-K}^{K} \frac{1}{\pi k} \sin(\pi k E(t)) e^{-j\pi k} e^{j2\pi f_p k t} \tag{3}$$

where f_p is the PWM sampling frequency.

Since the imaginary part of (3) is an odd function, $E_{PFS,K}(t)$ is purely real. The finite number of terms used in the PFS can make the modulated amplitude a bandlimited signal and reduce the aliasing error. The unfiltered PFS of DPWM has excellent frequency-domain behavior as the

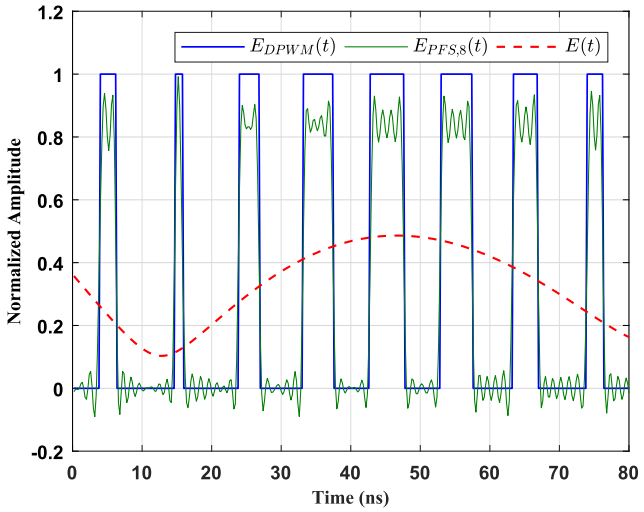

FIGURE 3. Comparison of conventional DPWM and PFS of DPWM with PWM sampling frequencies $f_p = 100$ MHz.

dynamic range is significantly increased leading to excellent ACLR as shown in Fig. 2. It can also be seen that increasing the number of terms K used in the PFS, which increases the bandwidth beyond the sampling frequency, would cause aliasing error as discussed in [10]. PFS of DPWM would become conventional DPWM in the frequency domain as K approaches infinity. The time-domain waveforms of conventional DPWM and PFS of DPWM are compared in Fig. 3. It can be seen that PFS of DPWM has ripples in the time domain and is no longer a two-level waveform. Those ripples are the result of Gibbs phenomenon and leads to distortion during nonlinear power amplification as shown in [11]. Moreover, the ripples may exceed unity which is normalized to the maximum PA input and requires back off of the PA leading to lower output power and efficiency.

In [15], it was stated that Gibbs phenomenon occurs near the discontinuity while using PFS to approximate a non-periodic or discontinuous function. It was shown by Gibbs in [24] that the peak amplitude does not decrease with increased terms in the Fourier series. It can be expressed as the form

$$\lim_{K\to\infty} |f(t) - f_K(t)| \neq 0, \tag{4}$$

where $f_K(t)$ is K-term PFS of a discontinuous function $f(t)$ such as a DPWM signal. An example is illustrated in Fig. 4 while $f(t)$ is a square wave with period T_p. It can be seen that PFS is not a good approximation of a discontinuous function because of Gibbs phenomenon. It can be proven that the ripples appear not because of limiting harmonics to finite numbers, but actually because of using Fourier series to approximate the original function.

III. GIBBS PHENOMENON REDUCTION FILTER

When using PFS $\hat{g}_K(t)$ to represent a 2π-periodic analytic function $\hat{g}(t)$, it is well known that the approximation error $|\hat{g}(t) - \hat{g}_K(t)|$ approaches zero with increasing K.

In contrast to perfect estimation of periodic analytic function, the PFS of discontinuous function suffers from Gibbs

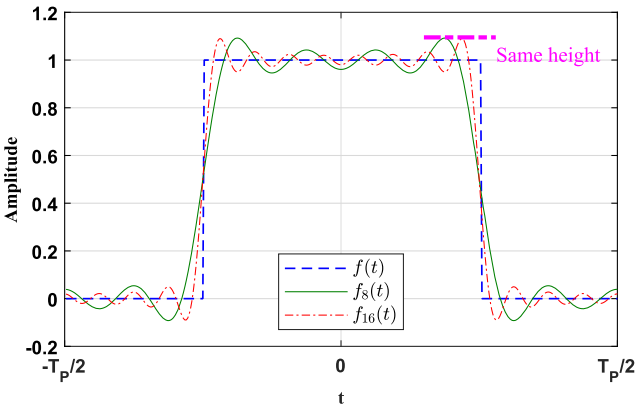

FIGURE 4. An illustration of Gibbs phenomenon in square wave that shows the approximation error would not reduce with higher order of Fourier series.

phenomenon because of poor convergence. To resolve this problem, adding an even function filter σ which has continuous 1st to $(p\text{-}1)^{\text{th}}$-order derivative can accelerate the rate of convergence. Any real and even function $\sigma(f)$ which meets the following properties (5)-(7) can be defined as a p^{th}-order filter.

$$\sigma(f) = 0, \quad |f| > 1 \tag{5}$$

$$\sigma(0) = 1, \quad \sigma(1) = 0 \tag{6}$$

$$\begin{cases} \sigma^{(n)}(0) = 0 \\ \sigma^{(n)}(1) = 0 \end{cases}, \quad \forall 1 \leq n \leq p-1 \tag{7}$$

Note that the superscript n in (7) indicates the n^{th}-order derivative of σ. The filter that only suffices (5) cannot improve the convergence since it is just the reduction of terms of a PFS. Because of (6) and (7), the filter is a continuous waveform that is essential for the filter to enhance approximation accuracy to higher orders. The filtered PFS of a 2π-period discontinuous function $f(t)$ with α discontinuity points $\xi_1 \sim \xi_\alpha$ can be redefined as

$$F_K(t) = \sum_{k=-K}^{K} c_k\,(f\,(t)) \cdot \sigma(\frac{k}{K}) e^{jkt} \tag{8}$$

where $c_k(f(t))$ is the FS coefficients of $f(t)$. The impulse response of filter σ in the time domain is defined as $\psi_K^0(t)$ and can be expand to higher order as

$$\psi_K^0(t) = \sum_{k=-K}^{K} \sigma(\frac{k}{K}) e^{jkt}, \tag{9}$$

where

$$\begin{cases} (\psi_K^n)' = \psi_K^{n-1} \\ \int_0^{2\pi} \psi_K^n(t)dt = 0 \end{cases}, \quad \forall n \geq 1 \tag{10}$$

while the superscript n of $\psi_K^n(t)$ means the n-th integral of $\psi_K^0(t)$, which would be later utilized for further analysis of (15). According to (8) and (9), the approximation $F_K(t)$ can be transformed into the convolution sum as

$$F_K(t) = \frac{1}{2\pi} \int_0^{2\pi} f(x)\psi_K^0(t-x)dx, \tag{11}$$

Moreover, (9) can also be expressed with Fourier transform through the periodic property as

$$\psi_K^0(t) = K \sum_{m=-\infty}^{\infty} \hat{\sigma}(Kt + 2mK\pi), \tag{12}$$

where $\hat{\sigma}(t)$ is the inverse Fourier transform of the filter $\sigma(f)$ and

$$\begin{aligned}\hat{\sigma}(t) &= \int_{-\infty}^{\infty} \sigma(f) e^{jxt} df = \int_{-1}^{1} \sigma(f) e^{jxt} df \\ &= \frac{j}{t} \int_{-1}^{1} \sigma(f)^{(1)} e^{jxt} df \\ &= \left(\frac{j}{t}\right)^2 \int_{-1}^{1} \sigma^{(2)}(f) e^{jxt} df \ldots \\ &= \left(\frac{j}{t}\right)^p \int_{-1}^{1} \sigma^{(p)}(f) e^{jxt} df. \end{aligned} \tag{13}$$

Note that the integral boundary of (13) can be modified to $[-1, 1]$ because of the filter property defined in (5). The integral result can be integrated by parts to higher-order derivative order p. It is easier to estimate the bounded value in the Fourier transform form, which would be derived later. Additionally, ripples appear in the time domain due to Gibbs phenomenon. For the bounded value calculation, ripples would not affect the result. For the convolution in (11), the ripples of $\psi_K^0(t)$ grow inversely to $f(t)$ near discontinuities which would suppress the approximation error. The condition in (10) defines the zero mean value to every order of integration. Because of (5) and (7), the FS in (9) can be rewritten as

$$\psi_K^0(t) = 1 + \sum_{k\neq 0} \sigma\left(\frac{k}{K}\right) e^{jkt}. \tag{14}$$

Subsequently, all the other integrations can be derived from $\psi_K^0(t)$ as

$$\begin{aligned}\psi_K^1(t) &= t - \pi + \sum_{k\neq 0} \frac{1}{jk} \sigma\left(\frac{k}{K}\right) e^{jkt} \\ \psi_K^2(t) &= \frac{1}{2}t^2 - \pi t + \frac{\pi^2}{3} + \sum_{k\neq 0} \frac{1}{(jk)^2} \sigma\left(\frac{k}{K}\right) e^{jkt} \\ \psi_K^n(t) &= B_n(t) + \sum_{k\neq 0} \frac{1}{(jk)^n} \sigma\left(\frac{k}{K}\right) e^{jkt}, \quad \forall n \geq 1 \end{aligned} \tag{15}$$

where $B_n(t)$ is the Bernoulli polynomial of degree n and can be expressed in FS as

$$\begin{aligned} B_1(t) &= \sum_{k\neq 0} \frac{j}{k} e^{jkt} \\ B_2(t) &= \sum_{k\neq 0} \frac{1}{k^2} e^{jkt} \\ B_n(t) &= \sum_{k\neq 0} \frac{j^{2-n}}{k^n} e^{jkt} = -\sum_{k\neq 0} \frac{1}{(jk)^n} e^{jkt}, \quad \forall n \geq 1 \end{aligned} \tag{16}$$

Therefore, $\psi_K^n(t)$ can be rewritten as

$$\psi_K^n(t) = \sum_{k\neq 0} \frac{1}{(jk)^n} \left[\sigma\left(\frac{k}{K}\right) - 1\right] e^{jkt}, \quad \forall n \geq 1 \tag{17}$$

Integrating the convolution sum in (11) by parts with the impulse response (9), the approximation error can be derived as

$$\begin{aligned} F_K(t) - f(t) = \frac{1}{2\pi} \sum_{m=1}^{\alpha} \sum_{k=0}^{p-1} D_{k,m}(t) \psi_K^{k+1}(t - \xi_m) \\ + \frac{1}{2\pi} \int_0^{2\pi} v_p(x) \psi_K^p(t - x) dx \end{aligned} \tag{18}$$

with $D_{k,m}(t)$ defined as the discontinuous difference of discontinuous points $(\xi_1 \sim \xi_\alpha)$ in $0\sim 2\pi$ period of $f(t)$ in the form of

$$D_{k,m} = \lim_{t\to\xi_m^+} f^{(k)}(t) - \lim_{t\to\xi_m^-} f^{(k)}(t). \tag{19}$$

The first term in the right-hand side of (18) can be defined as the discontinuity error. It can be seen that the impulse response of the filter can recover the singularity in every order derivative of $f(t)$. The second term in the right-hand side of (18) is the convolution of $v_p(t)$ and $\psi_K^p(t)$, which is the p^{th}-order derivative of $f(t)$ without considering singular points and the p-th integration of $\psi_K^0(t)$, respectively. It is easy to prove that the convolution of $v_p(t)$ and $\psi_K^p(t)$ is bounded by K^{1-2p} where the detailed derivation is shown in Appendix A.

Since the second term in the right-hand side of (18) can be bounded by power of K^{1-2p}, the discontinuity error plays a dominant role in the convergence of the approximation error. To estimate the convergence of the discontinuity error, it is important to find the boundary of $\psi_K^n(t)$ for $n > 0$, which should start from $\psi_K^0(t)$ such that

$$\left|\psi_K^0(t)\right| \leq C_0 \cdot K^{1-p} \left\|\sigma^{(p)}\right\|_{L^2(0,1)} \left\{t^{-p} + (2\pi - t)^{-p}\right\} \tag{20}$$

where C_0 is a constant independent of K, p, σ, t and the norm of σ is defined as

$$\left\|\sigma^{(p)}\right\|_{L^2(0,1)} = \left[\int \left|\sigma^{(p)}(t)\right|^2 dt\right]^{\frac{1}{2}}. \tag{21}$$

The derivation of (20) is detailed in Appendix B. It is also proved that $\psi_K^0(t)$ has the most significant influence on the convergence compared to other integrations $\psi_K^n(t)$, $\forall n \geq 1$. The approximation error can then be derived as

$$\begin{aligned} |F_K(t) - f(t)| &\leq \sum_{m=1}^{\alpha} C \cdot K^{1-\mathrm{p}} (\Delta t)^{1-p}, \\ \Delta t &= \begin{cases} t - \xi_m, t \geq \xi_m \\ t + 2\pi - \xi_m, t < \xi_m \end{cases} \end{aligned} \tag{22}$$

The result can be regarded as: for any filter satisfying the definition from (5)-(7) with $p \geq 2$, it can let $F_K(t)$ converge to $f(t)$ uniformly with power K^{1-p} in the set such that the distance to the discontinuous points Δt are greater than $K^{-1+\varepsilon}$

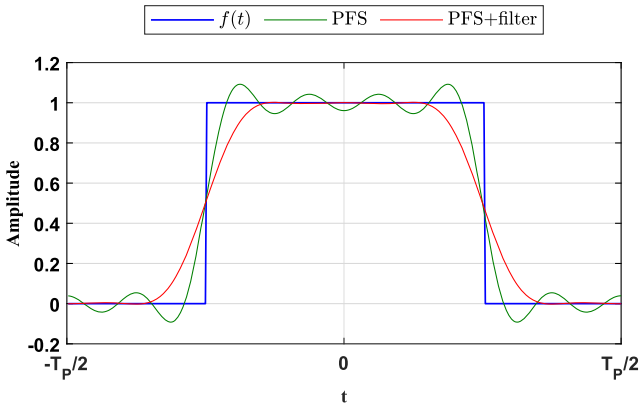

FIGURE 5. A comparison of two approximations with and without the Gibbs phenomenon reduction filter with $K = 8$.

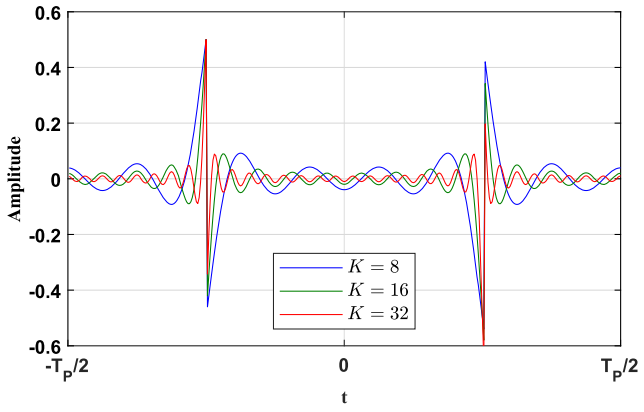

FIGURE 6. The approximation error of PFS with different K.

for every $\varepsilon > 0$. The minimum error can be achieved by minimizing C in (22). In [16], a possible filter σ was proposed as

$$\sigma(f) = 1 - \frac{(2p-1)!}{(p-1)!^2} \int_0^f [t(1-t)]^{p-1} dt \tag{23}$$

such that the norm in (21) and C in (22) are minimized.

For the case of square waves, since our application is PWM, (18) can be reduced to the following form

$$F_K(t) - f(t) = \frac{1}{2\pi} \left[\psi_{\mathrm{K}}^1 (t - \xi_1) - \psi_{\mathrm{K}}^1 (t - \xi_2) \right] \tag{24}$$

Since there is only ψ_K^1 in (24), there is no need to approximate the original function to higher-order derivative. Hence the minimum value of $p = 2$ should be selected to minimize the approximation error in (24). The Gibbs phenomenon reduction filter implemented for square waves and PWM can then be derived from (23) as

$$\sigma_{\mathrm{GR}}(f) = 1 - 3f^2 + 2f^3. \tag{25}$$

To examine the effect of the Gibbs phenomenon reduction filter, simulations of a 50% duty cycle square wave with period T_p and two different approximations both using $K = 8$ are performed. The comparison of three types of waveforms are shown in Fig. 5 and the approximation error of the PFS and $F_K(t)$ with increasing K are shown in Figs. 6 and 7,

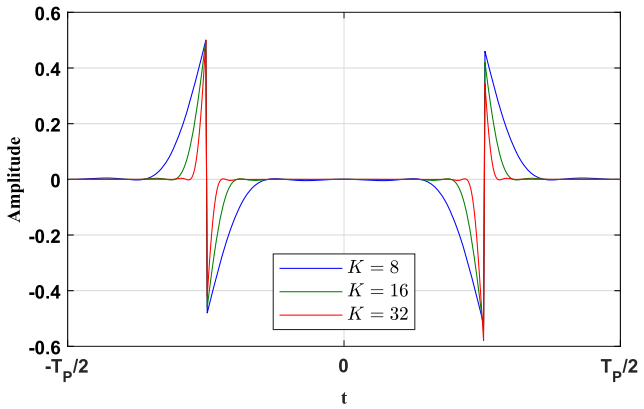

FIGURE 7. The approximation error of $F_K(t)$ with different K.

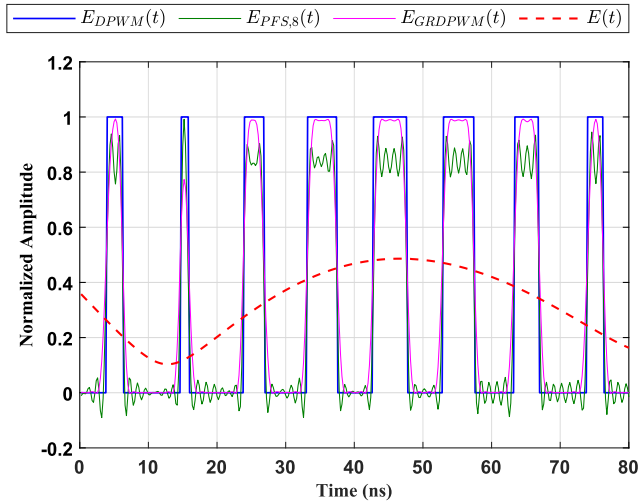

FIGURE 8. Comparison of conventional DPWM, unfiltered and filtered PFS of an envelope signal in the time domain with PWM sampling frequencies $f_p = 100$ MHz.

respectively. As shown in Fig. 6, the PFS suffers from poor convergence and the ripples will always exist regardless of the order. On the other hand, it is shown in Figs. 5 and 7 that the proposed $F_K(t)$ has decent approximation in the set $K^{-1+\varepsilon}$ away from the discontinuity for every $\varepsilon > 0$. Although the set $\{\Delta t \leq K^{-1}\}$ does not converge uniformly, it is either strictly increasing or decreasing from the point of discontinuity. In other words, the approximation error in the set $\{\Delta t \leq K^{-1}\}$ would not decrease with the increase of K while the maximum error occurs at the discontinuity whose approximate value is the average of both sides.

The Gibbs-phenomenon-reduced digital pulse-width modulation (GRDPWM), which reduces the time-domain ripples in PFS of DPWM by adding the proposed Gibbs phenomenon reduction filter in (25), has the form of

$$E_{GRDPWM}(t) = \sum_{k=-K}^{K} \left\{ \frac{1}{\pi k} \sin(\pi k E(t)) e^{-j\pi k} e^{j2\pi f_p k t} \cdot \left[1 - 3\left(\frac{k}{K}\right)^2 + 2\left(\frac{k}{K}\right)^3 \right] \right\} \tag{26}$$

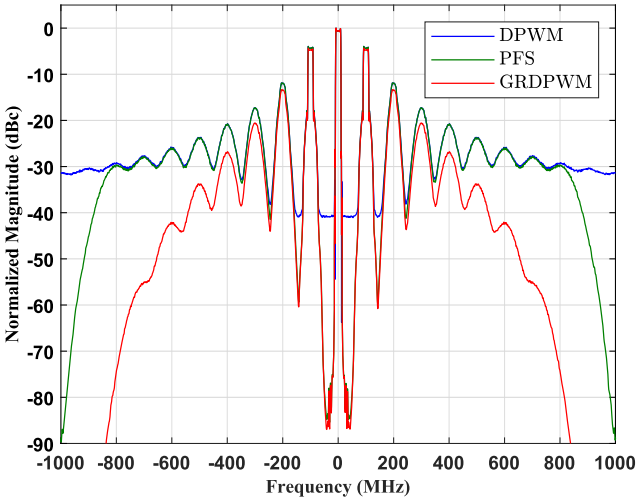

FIGURE 9. Comparison of the wideband spectra for a 20-MHz 5G NR signal between conventional DPWM, unfiltered and filtered PFS of DPWM with PWM sampling frequencies $f_p = 100$ MHz and a span of 2 GHz.

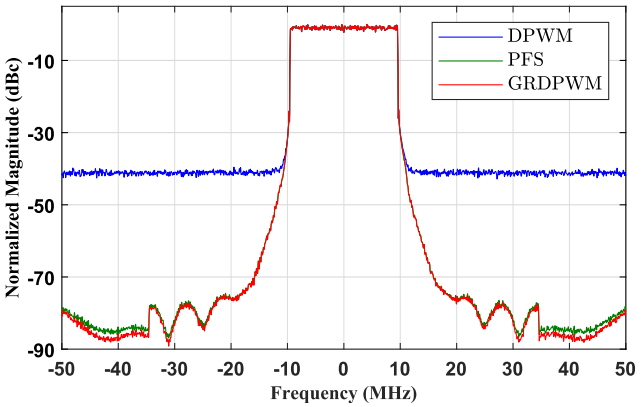

FIGURE 10. Comparison of the spectra for a 20-MHz 5G NR signal between conventional DPWM, unfiltered and filtered PFS of DPWM with PWM sampling frequencies $f_p = 100$ MHz and a span of 100 MHz.

It is obvious that the computational resources of adopting the filter is negligible compared to the calculation of PFS, which is only multiplying K constants. Fig. 8 compares the three types of PWM all using $f_p = 100$ MHz for a 20-MHz 5G NR signal with $K = 8$ for unfiltered and filtered PFS of DPWM as in [10] and [11]. It can be seen in Fig. 8 that with the addition of the Gibbs phenomenon reduction filter, voltage ripples are significantly reduced. In Figs. 9 and 10, wideband and narrowband spectral performances are compared, respectively. From (26) and Fig. 10, it can be seen that the Gibbs phenomenon reduction filter only reduces the amplitude of the harmonics. Therefore, ACLR performances of unfiltered and filtered PFS of DPWM are identical. For the results in Fig. 10, both unfiltered and filtered PFS of DPWM achieved ACLR performance of -53.4 dBc while the ACLR of conventional DPWM was only -39.9 dBc.

To demonstrate the benefits of using the proposed GRDPWM, a static polynomial model based on characterization of the PA reported in [25] was used for simulation. The AM-AM characteristics of the PA reported in [25] is shown in Fig. 11. The PA was designed for high efficiency and not for linearity. Therefore, the PA has low gain for small inputs because of under biasing and is compressed for large inputs. Simulations were carried out for both unfiltered and filtered PFS of DPWM, which are shown in Figs. 12 and 13, respectively. It is clear that time-domain ripples become distorted for unfiltered PFS of DPWM while the proposed GRDPWM appears to be more immune to PA distortion. The calculated rms errors for unfiltered and filtered PFS of DPWM are 4.57% and 3.60% after distortion from nonlinear amplifications, respectively.

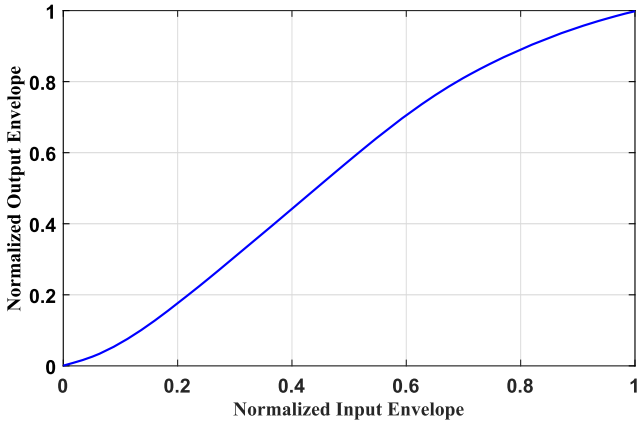

FIGURE 11. The measured AM-AM characteristics of the RF PA reported in [25].

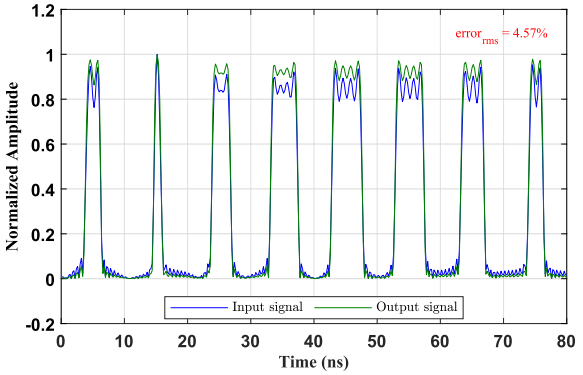

FIGURE 12. Simulated normalized envelope of unfiltered PFS of DPWM before and after the AM-AM model.

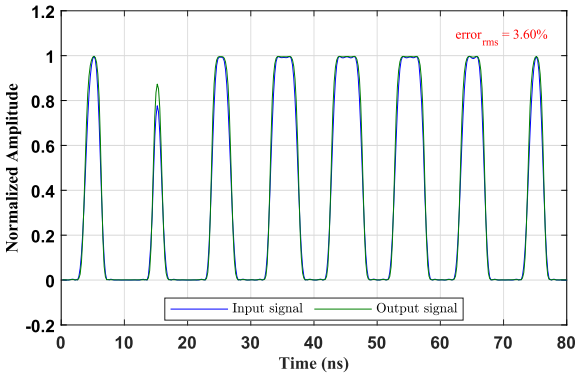

FIGURE 13. Simulated normalized envelope of proposed GRDPWM or filtered PFS of DPWM before and after the AM-AM model.

TABLE 1. Performance Comparison of Conventional IQ signal, DPWM, PFS and GRDPWM.

	This work	This work	[10]	[11]	[12]	This work	[26]	This work
Technique	Conventional IQ	DPWM	PFS	PFS	PFS	PFS	MD-PWMT	GRDPWM
Standards	NR DL 20 MHz	NR DL 20 MHz	5 MHz	LTE DL 20 MHz	LTE DL 20 MHz	NR DL 20 MHz	LTE UL 20 MHz	NR DL 20 MHz
PA Class	E	E	AB	C	C	E	D	E
Freq. (MHz)	2140	2140	900	836.5	2140	2140	640	2140
PAPR (dB)	8.5	8.5	7	7.5	7.5	8.5	-/-	8.5
P_{avg} (dBm)	19.2	17.4	-/-	20.1	35.1	16.8	25.4	18.0
Peak power (dBm)	26.0	26.0	39.1	29.5	41.8	26.0	27.8	26.0
ACLR (dBc)	-24.9	-33.1	≈ -37.0	-32.2	-40.1	-35.5	-30.5	-45.4
EVM (%)	12.8	4.30	-/-	-/-	-/-	3.34	8.8	1.67
η_{avg} (%)	38.7	23.3	33.6	24.4	30.5	22.7	16.1	28.3
η_{peak} (%)	63.9	63.9	72	70	68.9	63.9	-/-	63.9
Digital implementation	No	Partial	No	No	No	No	All	No

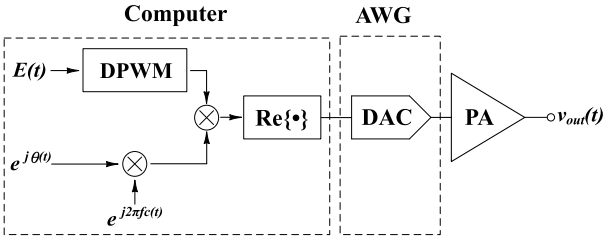

FIGURE 14. Basic block diagram of the implemented PMPT system.

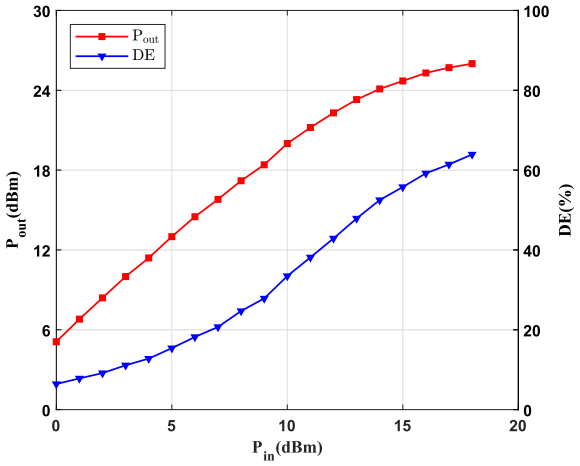

FIGURE 15. The measured output power and efficiency with varying input power.

IV. SYSTEM IMPLEMENTATION AND MEASUREMENT

For validation of the proposed GRDPWM, a prototype transmitter was implemented. The basic block diagram of the implemented PMPT is shown in Fig. 14. The PFS signal filtered with the proposed Gibbs phenomenon reduction filter is generated and up-converted to the desired carrier frequency digitally and loaded into an arbitrary waveform generator (AWG). To achieve the goal of reducing envelope and phase distortion caused by matching bandwidth as discussed in [11], A broadband matching PA that was designed in [25] was utilized in this work. Using the ATF-511P8 enhancement-mode pHEMT transistor, the PA was designed with 1.2 GHz bandwidth from 1.4 to 2.6 GHz with efficiencies of over 57% throughout the designed bandwidth. The measured characteristics with varying input power at a center frequency of 2.14 GHz is shown in Fig. 15. It can achieve a maximum output power of 26.0 dBm with a peak drain efficiency of 63.9%.

The test signal used in this work is a 256-QAM 5G NR signal with a 20-MHz bandwidth and a 8.5 dB PAPR, which is the most challenging signal currently defined by the sub-6-GHz 3GPP 5G NR standard. To compare the distortion after nonlinear power amplification, different types of DPWM with 100 MHz PWM frequencies and conventional IQ data without PWM were used in the proposed PMPT system with a carrier frequency of 2.14 GHz. The measured spectral performances of conventional IQ, DPWM, PFS and GRDPWM are measured with a spectrum analyzer and compared in Fig. 16. The measured AM-AM and AM-PM performances are shown in Figs. 17 and 18, respectively. Table 1 summarizes the detailed performances of different setups of the prototype transmitter and the works proposed in [10]–[12] and [26]. To compare the linearity fairly, peak power is set to same level in each technique in this work and measured with an RF power meter. Therefore the average output power varies in Table 1. Moreover, all methods are tested under the same bias condition for the measurements of AM-AM characteristics shown in Figs. 11 and 17. The

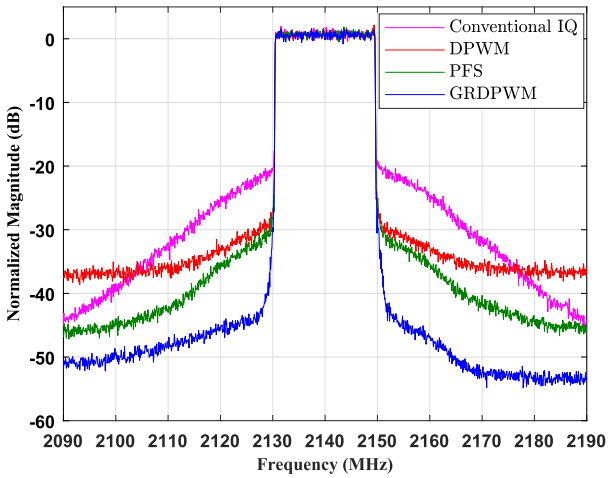

FIGURE 16. The measured output spectrum comparison of conventional IQ signal, DPWM, PFS and GRDPWM.

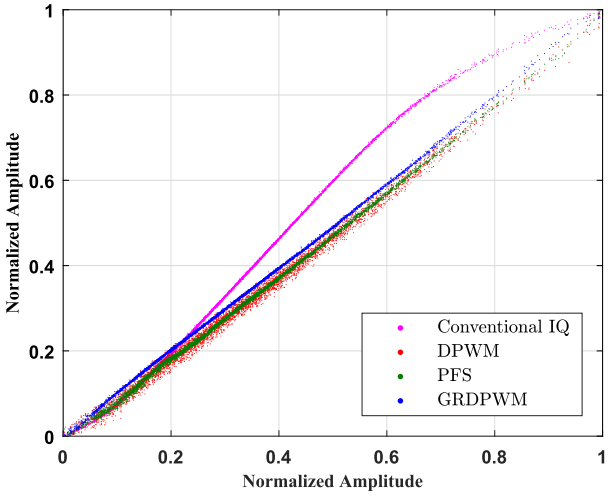

FIGURE 17. The measured AM-AM comparison of conventional IQ signal DPWM, PFS and GRDPWM.

results validate our hypothesis that PMPT can obtain better linearity performance than conventional IQ which benefits from overdriving and operating the PA as a switch. Among the various DPWM methods, conventional DPWM suffers from aliasing and can be clearly seen from the higher noise floor away from the carrier frequency. Unfiltered PFS alleviates the aliasing problem as seen from the lowered noised floor. However, from the spectral regrowth in the adjacent channels, the unfiltered PFS signal has linearity issues. Moreover, back off has to be performed on the unfiltered PFS signal to avoid hard-clipping of the ripples in the signal. As a result, the output power is reduced and efficiency is degraded. The proposed GRDPWM or filtered PFS signal is more immune to PA nonlinearity and shows the best linearity performance among all cases. Without the ripples, the RF PA can be driven harder and thus have higher output power and efficiency. Since the proposed GRDPWM is more immune to PA nonlinearity, the PMPT is able to achieve an ACLR of -45.4 dBc, which exceeds the base station linearity

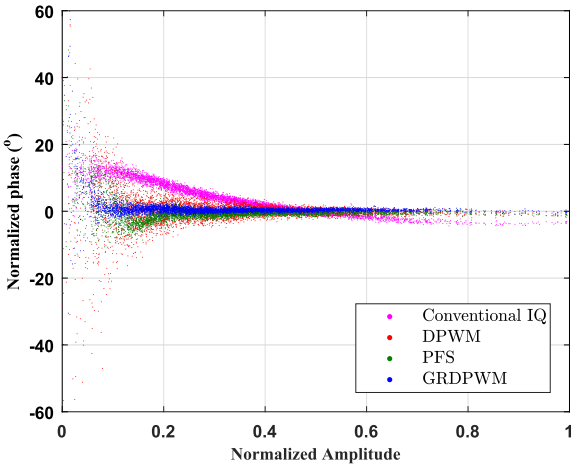

FIGURE 18. The measured AM-PM comparison of conventional IQ signal, DPWM, PFS and GRDPWM.

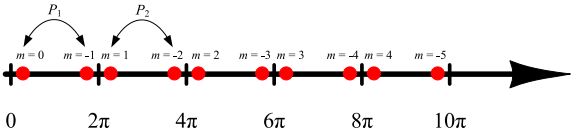

FIGURE 19. Location of $(t + 2m\pi)$.

specifications for the 5G NR standard without using any DPD techniques. Moreover, an error vector magnitude (EVM) of 1.67% is achieved, which exceeds the 3.5% specification for 256-QAM modulation.

V. CONCLUSION

In this paper, the problems raised by using PFS of DPWM in PMPTs because of Gibbs phenomenon are discussed. The analysis results show that by adding a proposed low-pass filter in the baseband, time-domain ripples are reduced effectively while not altering the performance in the frequency domain. For validation, the proposed GRDPWM signal for a 20-MHz 256-QAM 5G NR signal is tested on a wideband PMPT system. Compared to using unfiltered PFS of DPWM, the measured ACLR improves by 10 dB and can achieve the spectral requirements of 5G NR base stations. The measured drain efficiency is also improved from 23.3% to 28.3% because back off is no longer required. Moreover, the proposed filter needs very little computational resources, which can be negligible compared to other linearization techniques and can be easily implemented in hardware.

APPENDIXES

APPENDIX A

According to the Cauchy-Schwarz inequality, the convolution of $v_p(t)$ and $\psi_K^p(t)$ can be bounded as

$$\left|\int_0^{2\pi} v_p(x)\psi_K^p(t-x)dx\right| \le \left[\int_0^{2\pi} \left|\psi_K^p(t)\right|^2 dt\right]^{\frac{1}{2}} \times \left[\int_0^{2\pi} \left|v_p(t)\right|^2 dt\right]^{\frac{1}{2}} \quad (27)$$

According to the (17), $\int_0^{2\pi} \left|\psi_K^p(t)\right|^2 dt$ can be derived as

$$\int_0^{2\pi} \left|\psi_K^p(t)\right|^2 dt = 2\pi \sum_{k=-K}^{K} \frac{\left[\sigma(\frac{k}{K})-1\right]^2}{k^{2p}} + 2\pi \sum_{|k|>K} \frac{1}{k^{2p}}$$
$$= 2\pi \left\{ K^{1-2p} \sum_{k=-K}^{K} A^2 \frac{1}{K} + \sum_{|k|>K} k^{-2p} \right\},$$
$$A = \left\{ \frac{\left[\sigma(\frac{k}{K})-1\right]}{\left(\frac{k}{K}\right)^p} \right\} \quad (28)$$

The first term of (28) is the Riemann sum of function and can be derived as an integral

$$K^{1-2p} \int_{-1}^{1} \left[\frac{\sigma(x)-1}{x^p}\right]^2 dx \quad (29)$$

with $x = k/K$. This term can be bounded by K^{1-2p} if and only if the function has finite energy as

$$\int_{-1}^{1} \left[\frac{\sigma(x)-1}{x^p}\right]^2 dx < \infty, \quad (30)$$

which can be proved easily from the filter's properties. The second term of (28) can be bounded by the same power of K as

$$\sum_{|k|>K} k^{-2p} \le 2 \int_K^{\infty} k^{-2p} dk = \frac{K^{1-2p}}{p-0.5} \quad (31)$$

According to the results from (27)-(29) and (31), the second term in the right-hand side of (18) can be bounded by power of K^{1-2p} and has exponential convergence as

$$\frac{1}{2\pi} \left| \int_0^{2\pi} v_p(t) \psi_K^p(x-t) dx \right|$$
$$\le C_0 \cdot K^{\frac{1}{2}-p} \left[\int_0^{2\pi} \left|v_p(t)\right|^2 dt \right]^{\frac{1}{2}}. \quad (32)$$

APPENDIX B

From (12), $|\psi_K^0(t)|$ can be bounded as

$$\left|\psi_K^0(t)\right| \le K \sum_{m=-\infty}^{\infty} \left|\hat{\sigma}(K(t+2m\pi))\right|, \quad (33)$$

where the boundary of $\left|\hat{\sigma}(t)\right|$ can be derived from (13) as

$$|\sigma(t)| \le \left\|\sigma^{(p)}\right\|_{L^2(-1,1)} |t|^{-p} = 2 \left\|\sigma^{(p)}\right\|_{L^2(0,1)} |t|^{-p} \quad (34)$$
$$\left\|\sigma^{(p)}\right\|_{L^2(0,1)} = \int \left[\left|\sigma^{(p)}(t)\right|^2 dt\right]^{\frac{1}{2}} \quad (35)$$

so (33) can be rewritten as

$$\left|\psi_K^0(t)\right| \le K \left\{ 2 \left\|\sigma^{(p)}\right\|_{L^2(0,1)} \sum_{m=-\infty}^{\infty} |(K(t+2m\pi))|^{-p} \right\} \quad (36)$$

Since t is the point inside the open interval between 0 and 2π, the location of $(t+2m\pi)$ of each value m can be illustrated as Fig. 19. As shown in Fig. 19, it can be divided into pairs P_h bounded in the open interval $(2(h-1)\pi, 2h\pi)$. Each pair has maximum value with the following situations $t \to 0$ or $t \to 2\pi$. For every pair $(P_h, h > 1)$, the maximum value can be bounded as $|(P_h)^{-p}| \le (2(h-1)\pi)^{-p} + (2h\pi)^{-p}$. So the (36) can be rewritten as

$$\left|\psi_K^0(t)\right| \le 2K^{1-p} \left\|\sigma^{(p)}\right\|_{L^2(0,1)} \left\{t^{-p} + (2\pi - t)^{-p} + C\right\} \quad (37)$$
$$C = \sum_{h=2}^{\infty} (P_h)^{-p} = (2\pi)^{-p} + 2\sum_{h=2}^{\infty} (2h\pi)^{-p} \quad (38)$$

Other n-th integrals can be derived from (37) as

$$\left|\psi_K^n(t)\right| \le 2C_n \cdot K^{1-p} \left\|\sigma^{(p)}\right\|_{L^2(0,1)} \left\{t^{n-p} + (2\pi - t)^{n-p}\right\},$$
$$\forall n \ge 1 \quad (39)$$

which has a lower maximum boundary compared to $|\psi_K^0(t)|$.

REFERENCES

[1] L. R. Kahn, "Single-sideband transmission by envelope elimination and restoration," *Proc. IRE*, vol. 40, no. 7, pp. 803–806, Jul. 1952.
[2] W. H. Doherty, "A new high efficiency power amplifier for modulated waves," *Proc. IRE*, vol. 24, no. 9, pp. 1370–1392, Nov. 1935.
[3] H. Chireix, "High power outphasing modulation," *Proc. IRE*, vol. 23, no. 11, pp. 1370–1392, Nov. 1935.
[4] C. Huang, S. He, and F. You, "Design of broadband modified class-J Doherty power amplifier with specific second harmonic terminations," *IEEE Access*, vol. 6, pp. 2531–2540, 2018.
[5] T. Sharma, P. Aflaki, M. Helaoui, and F. M. Ghannouchi, "Broadband GaN class-E power amplifier for load modulated delta sigma and 5G transmitter applications," *IEEE Access*, vol. 6, pp. 4709–4719, 2018.
[6] Z. Yang, Y. Yao, Z. Liu, M. Li, T. Li, and Z. Dai, "Design of high efficiency broadband continuous class-f power amplifier using real frequency technique with finite transmission zero," *IEEE Access*, vol. 6, pp. 61983–61993, 2018.
[7] Y. Wang, "An improved Kahn transmitter architecture based on delta-sigma modulation," in *IEEE MTT-S Int. Microw. Symp. Dig.*, vol. 3, Jun. 2003, pp. 1327–1330.
[8] J.-H. Chen, H.-S. Yang, and Y.-J. E. Chen, "A multi-level pulse-modulated polar transmitter using digital pulse-width modulation," *IEEE Microw. Wireless Compon. Lett.*, vol. 20, no. 5, pp. 295–297, May 2010.
[9] K.-F. Liang, H.-S. Yang, C.-W. Chang, and J.-H. Chen, "A wideband pulse-modulated polar transmitter using envelope correction for LTE applications," *IEEE Trans. Microw. Theory Techn.*, vol. 62, no. 8, pp. 2603–2608, Aug. 2015.
[10] K. Hausmair, S. Chi, P. Singerl, and C. Vogel, "Aliasing-free digital pulse-width modulation for burst-mode RF transmitters," *IEEE Trans. Circuits Syst. I, Reg. Papers*, vol. 60, no. 2, pp. 415–427, Feb. 2013.
[11] J.-H. Chen, C.-W. Chang, and H.-S. Yang, "Linearity enhanced wide-bandwidth pulse-modulated polar transmitters for LTE femtocell applications," *IEEE Trans. Microw. Theory Techn.*, vol. 64, no. 1, pp. 219–225, Jan. 2016.
[12] C.-W. Chang, S.-C. Lin, J.-H. Chen, and J. Staudinger, "A highly linear pulse-modulated polar transmitter using aliasing-free digital PWM for small-cell base stations," *IEEE Microw. Wireless Compon. Lett.*, vol. 28, no. 8, pp. 729–731, Aug. 2018.
[13] J.-H. Chen, H.-S. Yang, H.-C. Lin, and Y.-J. E. Chen, "A polar-transmitter architecture using multiphase pulsewidth modulation," *IEEE Trans. Circuits Syst. I, Reg. Papers*, vol. 58, no. 2, pp. 244–252, Feb. 2011.
[14] C.-W. Chang, S.-C. Lin, J.-H. Chen, and J. Staudinger, "A multi-level pulse-modulated polar transmitter based on Doherty power amplifier and memoryless digital predistortion," *IEEE Microw. Wireless Compon. Lett.*, vol. 28, no. 10, pp. 933–935, Oct. 2018.
[15] A. V. Oppenheim, A. S. Willsky, and S. Hamid, *Signals and Systems*, 2nd ed. Upper Saddle River, NJ, USA: Prentice-Hall, 1983.
[16] H. Vandeven, "Family of spectral filters for discontinuous problems," *J. Sci. Comput.*, vol. 6, no. 2, pp. 159–192, Jun. 1991.

[17] D. Gottlieb, C. W. Shu, A. Solomonoff, and H. Vandeven, "On the Gibbs phenomenon I: Recovering exponential accuracy from the Fourier partial sum of a non-periodic analytic function," *J. Comput. Appl. Math.*, vol. 43, nos. 1–2, pp. 81–98 Nov. 1991.
[18] D. Gottlieb and C.-W. Shu, "On the Gibbs phenomenon and its resolution," *SIAM Rev.*, vol. 39, no. 4, pp. 644–668, Dec. 1997.
[19] B. D. Shizgal and J.-H. Jung, "Towards the resolution of the Gibbs phenomena," *J. Sci. Comput.*, vol. 161, no. 1, pp. 41–65, Dec. 2003.
[20] A. Gelb and S. Gottlieb, "The resolution of the Gibbs phenomenon for Fourier spectral methods," in *Advanced in Gibbs Phenomenon*, A. J. Jerri, Ed. Potsdam, NY, USA: Sampling, Dec. 2006.
[21] Z. Song and D. V. Sarwate, "The frequency spectrum of pulse width modulated signals," *Signal Process.*, vol. 83, no. 1, pp. 2227–2258, Oct. 2003.
[22] D. G. Holmes and T. A. Lipo, *Pulse Width Modulation for Power Converters: Principles and Practice*. Piscataway, NJ, USA: IEEE Press, 2003. [Online]. Available: https://ieeexplore.ieee.org/book/5264450
[23] R. Guinee, "A novel Fourier series simulation tool for pulsewidth modulation (PWM) in pulsed power systems," in *Proc. 22nd IEEE Symp. Fusion Eng.*, Jun. 2007, pp. 1–4.
[24] J. W. Gibbs, "Fourier series," *Nature*, vol. 606, p. 200, Apr. 1899.
[25] S.-C. Lin, Y.-C. Hsieh, S.-H. Xu, and J.-H. Chen, "A highly efficient pulse-modulated polar transmitter using broadband class E power amplifier for femtocell base stations," in *Proc. IEEE Asia–Pacific Micro. Conf.*, Nov. 2018, pp. 64–66.
[26] M. T. Pasha, M. F. U. Haque, J. Ahmad, and T. Johansson, "A modified all digital polar PWM transmitter," *IEEE Trans. Circuits Syst. I, Reg. Papers*, vol. 65, no. 2, pp. 758–768, Feb. 2018.

SHU-CHEN LIN received the B.S. degree in engineering science and ocean engineering from National Taiwan University, Taipei, Taiwan, in 2015, where he is currently pursuing the Ph.D. degree.

From 2015 to 2018, he was a Research Assistant with the Department of Engineering Science and Ocean Engineering, where he was involved in RF power amplifiers linearization for 4G/5G wireless infrastructure. In 2019, he joined NanoSemi, Inc., Waltham, MA, USA, where he is currently an Intern Engineer. His current research interests include use of signal processing strategies for linearity improvement of RF power amplifiers and high-efficiency transmitters in wireless communication systems.

SHUO-HENG XU received the B.S. degree in engineering science and ocean engineering from National Taiwan University, Taipei, Taiwan, in 2017, where he is currently pursuing the Ph.D. degree.

Since 2017, he has been a Graduate Research Assistant with the Department of Engineering Science and Ocean Engineering, National Taiwan University. His current research interests include analog integrated circuit design and high-efficiency transmitters in wireless communication systems.

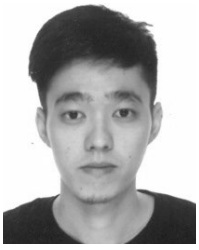

YOU-HUEI CHEN received the B.S. degree in electronic and computer engineering from the National Taiwan University of Science and Technology, Taipei, Taiwan, in 2012, and the M.S. degree in electronic engineering from National Taiwan University, Taipei, in 2016.

From 2016 to 2018, he was a Hardware Engineer with Himax Technology, Taipei, where he was involved with image processing IP and hardware/software co-design. In 2018, he joined the Department of Engineering Science and Ocean Engineering, National Taiwan University, where he is currently a Research Engineer. His current research interests include wireless communication, reconfigurable hardware accelerator architectures, and digital micromirror device (DMD) applications.

CHUN-WEI CHANG (S'15–M'19) received the M.S. and Ph.D. degrees in engineering science and ocean engineering from National Taiwan University, Taipei, Taiwan, in 2011 and 2018, respectively.

From 2011 to 2014, he was a Design Engineer with Richwave Technology, Taipei, where he was involved in designing RF components and CMOS FM receivers. From 2015 to 2017, he was an Intern Design Engineer with NXP Semiconductors, where he was involved in designing high-power RF power amplifiers for 4G/5G wireless infrastructure. In 2018, he joined NXP Semiconductors, Chandler, AZ, USA, where he is currently an RF/Wireless Development Engineer. He holds two issued U.S. and Foreign patents. His current research interests include analog/RF IC design, advanced receiver/transmitter architectures, and PA linearization techniques for cellular networks.

YI-JAN EMERY CHEN (S'97–M'01–SM'07–F'18) received the B.S. degree in electrical engineering from National Taiwan University, Taipei, Taiwan, in 1987, the M.S. degree in electrical and computer engineering from the University of California at Santa Barbara, CA, USA, in 1991, and the Ph.D. degree in electrical engineering from the Georgia Institute of Technology, Atlanta, in 2001.

From 1992 to 1993, he was a Software Engineer with Siemens Telecommunication, where he was involved with synchronous optical network (SONET) equipment development. From 1993 to 1996, he was with Tektronix, where he was responsible for electronic test and measurement solutions. From 2000 to 2002, he was with National Semiconductor, where he was involved with radio-frequency (RF) transceiver and RF power amplifier (PA) design. In 2002, he was with the Georgia Institute of Technology as a Member of the Research Faculty. Since 2003, he has been with National Taiwan University, where he is currently a Professor. His recent research focuses on the design of RF integrated circuits (RFICs), RF power amplifiers, LCD/LED drivers, and power management ICs. He is also a member of the IEEE Microwave Theory and Techniques Society (IEEE MTT-S) TC-26 Wireless Energy Transfer and Conversion Committee. He was a co-recipient of the 2000 IEEE MTT-S IMS Best Student Paper Award and the 2008 University Team Award for Contribution to Industrial Economics from the Ministry of Economic Affairs, Taiwan. He has been an Advisor of several student award recipients, including the Chi-Mei Award, the Macronix Golden Silicon Award, the Paper Award from the Institute of Chinese Electrical Engineering, and the Master Thesis Award from Taiwan IC Design Society. He has been serving on the Technical Program Committees of the IEEE MTT-S International Microwave Symposium (IMS) and the IEEE Radio and Wireless Symposium (RWS), since 2008. He has served as an Associate Editor for the IEEE Microwave and Wireless Components Letters, from 2009 to 2015.

JAU-HORNG CHEN (M'09–SM'19) received the B.S. degree in electrical engineering from National Taiwan University, Taipei, Taiwan, in 2001, and the M.S. and Ph.D. degrees in electrical and computer engineering from the Georgia Institute of Technology, Atlanta, GA, USA, in 2002 and 2006, respectively.

From 2006 to 2008, he was a Design Engineer with Freescale Semiconductor, Tempe, AZ, USA, where he was involved in designing dc–dc converters and digital predistortion linearizers for cell phone power amplifiers (PAs). In 2008, he returned to National Taiwan University, where he is currently a Full Professor and the Associate Chair of the Department of Engineering Science and Ocean Engineering. He holds five U.S. patents. His current research interests include analog/RF IC design, high-efficiency PAs, and FPGA prototyping.